

Physico-chemical and biological studies on three-dimensional porous silk/spray-dried mesoporous bioactive glass scaffolds

Arunseshan Chandrasekaran^{a,b,c,1}, Giorgia Novajra^{b,1}, Irene Carmagnola^c, Piergiorgio Gentile^d, Sonia Fiorilli^b, Marta Miola^b, Manjunatha Boregowda^e, Arivuoli Dakshanamoorthy^a, Gianluca Ciardelli^c, Chiara Vitale-Brovarone^{b,*}

^a Crystal Growth Centre, Anna University, Chennai, India

^b Department of Applied Science and Technology, Politecnico di Torino, Italy

^c Department of Mechanical and Aerospace Engineering, Politecnico di Torino, Italy

^d School of Mechanical and Systems Engineering, Newcastle University, Newcastle, UK

^e Department of Sericulture, University of Mysore, Mysore, India

ARTICLE INFO

Article history:

Received 12 February 2016

Received in revised form

27 April 2016

Accepted 26 May 2016

Available online 27 May 2016

Keywords:

Silk fibroin

Mesoporous bioactive glass

Composite scaffolds

Bone tissue engineering

ABSTRACT

The incorporation of a bioactive inorganic phase in polymeric scaffolds is a good strategy for the improvement of the bioactivity and the mechanical properties, which represent crucial features in the field of bone tissue engineering. In this study, spray-dried mesoporous bioactive glass particles (SD-MBG), belonging to the binary system of SiO₂-CaO (80:20 mol%), were used to prepare composite scaffolds by freeze-drying technique, using a silk fibroin matrix. The physico-chemical and biological properties of the scaffolds were extensively studied. The scaffolds showed a highly interconnected porosity with a mean pore size in the range of 150 μm for both pure silk and silk/SD-MBG scaffolds. The elastic moduli of the silk and silk/SD-MBG scaffolds were 1.1 ± 0.2 MPa and 6.9 ± 1.0 MPa and compressive strength were 0.5 ± 0.05 MPa and 0.9 ± 0.2 MPa, respectively, showing a noticeable increase of the mechanical properties of the composite scaffolds compared to the silk ones. The contact angle value decreased from 105.3° to 71.2° with the incorporation of SD-MBG particles. Moreover, the SD-MBG incorporation countered the lack of bioactivity of the silk scaffolds inducing the precipitation of hydroxyapatite layer on their surface already after 1 day of incubation in simulated body fluid. The composite scaffolds showed good biocompatibility and a good alkaline phosphatase activity toward human mesenchymal stromal cells, showing the ability for their use as three-dimensional constructs for bone tissue engineering.

© 2016 Elsevier Ltd and Techna Group S.r.l. All rights reserved.

1. Introduction

Bone is a connective tissue with high mechanical resistance derived by its unique design, in which cells are encased in a composite matrix essentially formed by inorganic apatite mineral phase and the organic phase of collagen [1]. The field of bone tissue engineering relies on biomaterial constructs that can offer a valid alternative for the current gold standard treatment i.e. autologous grafts. Scaffolds act as an engineered three dimensional (3D) porous structure that mediates cellular behavior and function, stimulating the replacement and regeneration of injured tissue and delivering biological molecules to the site of interest [2].

The design of bioartificial scaffolds which can combine the properties of organic and inorganic materials, is the aim of the biomimetic strategy in the field of bone tissue engineering [3].

Bombyx mori silk is also termed as mulberry silk. It is made up of globular glue like hydrophilic sericin coated over silk fibroin fibers. The sericin is a highly hydrophilic protein, which covers the silk fibroin fibers. It consists of 18 amino acids and has a molecular weight ranging from 24 to 400 kDa. The high solubility of sericin in aqueous solution limits its application in biomedical field [4,5]. Biopolymers have a low mechanical stability, hence improving the mechanical properties of the biopolymers is essential. Silk fibroin from *B. mori* is a natural biopolymer made up of 45.9% glycine, 30.3% alanine, 12.1% serine, 5.3% tyrosine, 1.8% valine, and only 4.7% of the other 15 amino acid types [6]. The recognized ability of silk fibroin for the fabrication of scaffolds, both by aqueous and organic solvents, made it a special material in tissue engineering as it is one of the few FDA approved biomaterial [7]. Silk fibroin is

* Corresponding author.

E-mail addresses: gianluca.ciardelli@polito.it (G. Ciardelli), chiara.vitale@polito.it (C. Vitale-Brovarone).

¹ The first two authors equally contributed to the manuscript.

widely used in biomedical applications both in the form of films [8] and 3D constructs [9], for different applications such as micropatterning [10] and microfluidics [11], implants [12] and drug delivery vehicles [13]. The β -sheet content and morphology of silk fibroin can be controlled by different post processing techniques such as ethanol treatment /autoclaving and the duration of these treatments allows the modulation of the crystal composition, structure, mechanical properties and the degradation rate. [14] However, the lack of bioactivity limited its use for the production of device for bone repair.

To overcome the lack of bioactivity, silk can be combined with inorganic bioactive materials such as calcium phosphate, hydroxyapatite and bioglass. Silk/nano calcium phosphate based composite scaffolds has shown good *in vitro* biocompatibility [15] and no degree of inflammation after 3 weeks of implantation *in vivo* with bone cells growing directly on the surface of the scaffolds [16]. Silk/hydroxyapatite composite scaffolds acted as a platform for the formation of new bone tissue thanks to the osteo-conductivity of the material that resulted in increased bone matrix production and secondly, by providing nucleation sites for the newly formed minerals [17,18]. On the other hand mesoporous bioactive glasses (MBGs) has been proposed for the preparation of silk-based composite scaffolds [19–22].

MBGs, developed in 2004 by Yan et al. [23], are glasses with composition similar to the conventional sol-gel glasses (SiO_2 -CaO- P_2O_5 or SiO_2 -CaO) that present ordered mesoporous channels (pore size ranging from 5 to 20 nm). Due to their high surface area and high pore volume MBGs induce accelerated bioactive responses and show the possibility to incorporate drug molecules, that can be subsequently released [20,21]. In the last decade, the role of mesoporous materials became significant in biomedical field and they were utilized as an effective drug delivery system [24] and as bone fillers [25]. Low mechanical strength, high brittleness and fast degradation rate are the major limiting factors that affect their employment in bone repair. MBGs have been conventionally produced by the combination of sol-gel technique, surfactant templating and evaporation induced self assembly (EISA), requiring a final step of grinding and sieving to obtain them in form of irregular shaped powders [19,21,22,26].

Wu et al. coated MBG scaffolds using silk, by incubating the MBG (molar ratio: Si/Ca/P=80/15/5) scaffolds in silk solution, showing improved attachment, proliferation and differentiation of Bone Mesenchymal Stem Cells (BMSC). The stable β -sheet structure of silk fibroin improved the relatively unstable MBG interface to support BMSC [21]. The *in vivo* osteogenic capacity of the same composite silk/MBG scaffolds was excellent in calvarial defects of mice [20]. A similar scaffold was utilized in calvarial defects to investigate drug delivery showing enhanced drug loading efficiency and release rate *in vitro* and promoted bone formation *in vivo* [27].

There is vast research interest in exploiting high surface area inorganic materials to improve the mechanical and biological property of composite materials. The chemical composition and shape of the inorganic phase play an important role on the final composite scaffold properties. The needle shaped calcium phosphate minerals improved the bioactivity and mechanical property of polymer based scaffolds [28]. Likewise, nanofiber morphology of bioglass showed to have greater bioactivity and mechanical stability compared with conventional bioglass [29]. Interestingly, spherical shaped bioactive glass microspheres showed to improve the mechanical and bioactivity of polymeric 2D structures [30]. Very recently aerosol-assisted methods have been proposed for the synthesis of mesoporous bioactive glass particles in the form of highly reproducible spherical shaped micron sized particles. The mean size and size distribution can be tuned acting on the composition and process parameters, in contrast to MBGs obtained by

conventional EISA method, which are obtained with more time-consuming processes and result in glass powders with irregular shape and larger, not homogeneous size after grinding [31]. The prepared spray dried mesoporous bioactive glass particles (80:20 mol% SiO_2 :CaO) have proved to improve the mechanical strength and the bioactivity of an injectable composite cement based on a calcium sulphate matrix [32].

In the present work, spray-dried mesoporous bioactive glass spherical particles with size in the range of few microns with narrow size distribution, prepared by combining sol-gel process and aerosol assisted spray-drying technique [25] (SD-MBG, 80:20 mol% of SiO_2 :CaO), were used for the first time to prepare composite silk-based scaffolds by freeze-drying. The spherical SD-MBG particles were used as the reinforcing inorganic phase in the polymer matrix. The possibility to control the particle morphology (i.e. size and shape) and its mesostructure is important for the development of more reproducible materials to be used as drug delivery system or as reinforcing phase in composite materials. The silk/SD-MBG composite scaffolds 10:1 (weight/weight) (Silk/SD-MBG) were characterized for their physico-chemical and mechanical properties. The bioactivity and biocompatibility of the composite scaffolds were also studied to evaluate the efficacy of the construct for bone tissue engineering.

2. Materials and methods

2.1. Materials

Silk cocoons of *B. mori* were obtained from the Department of Sericulture, University of Mysore, Karnataka. Sodium carbonate (Na_2CO_3 , $\geq 99.5\%$), calcium chloride (CaCl_2 , $\geq 95\%$), ethanol ($\text{C}_2\text{H}_5\text{OH}$, $\geq 99.8\%$) and dialysis tubing cellulose membrane (MWCO - 14,000) were purchased from Sigma-Aldrich. All chemicals used for SD-MBG synthesis were purchased from Sigma-Aldrich. All materials and chemicals were used as received, without any additional purification.

2.2. Methods

2.2.1. Preparation of the regenerated silk fibroin (RSF) solution

5 g of *B. mori* cocoons were cut into small pieces and boiled in 2 L of 0.02 M sodium carbonate solution for 40 min. The fibroin threads obtained, devoid of sericin, was thoroughly washed with deionized water and dried overnight. The dried fibroin was dissolved with 9.3 M lithium bromide solution at 70 °C for 4 h. The viscous sol obtained after dissolution was dialyzed against deionized water for 48 h to remove the salts. 0.5 mL of the obtained regenerated silk fibroin (RSF) solution was placed in a weighing boat and allowed to dry overnight under hood at room temperature to estimate the concentration of the solution, and, if needed, adjusted to be 6% (w/v) by diluting with deionized water [33].

2.2.2. Synthesis of spray-dried mesoporous bioactive glass (SD-MBG)

SD-MBG was synthesized by combining the sol-gel method with the aerosol-assisted spray drying technique using the protocol reported elsewhere [32]. The sol was prepared by dissolving 2.2 g of Pluronic P123 in 8.0 g of ethanol while 10.4 g of TEOS (tetraethyl orthosilicate) were pre-hydrolyzed for 20 min with 5.4 g of diluted hydrochloric acid (pH 2) and 12.0 g of ethanol. The two solutions were mixed together and stirred for 20 min, while 2.95 g of calcium nitrate tetrahydrate ($\text{Ca}(\text{NO}_3)_2 \cdot 4\text{H}_2\text{O}$, CaNT) was pre-dissolved in 3.4 g of ethanol. Finally, the CaNT solution was poured into the prepared sol. This final solution was mixed for at least 20 min before spraying, using the Mini Spray-Dryer B-290, equipped with the Inert-Loop B-295 (both from Büchi), needed

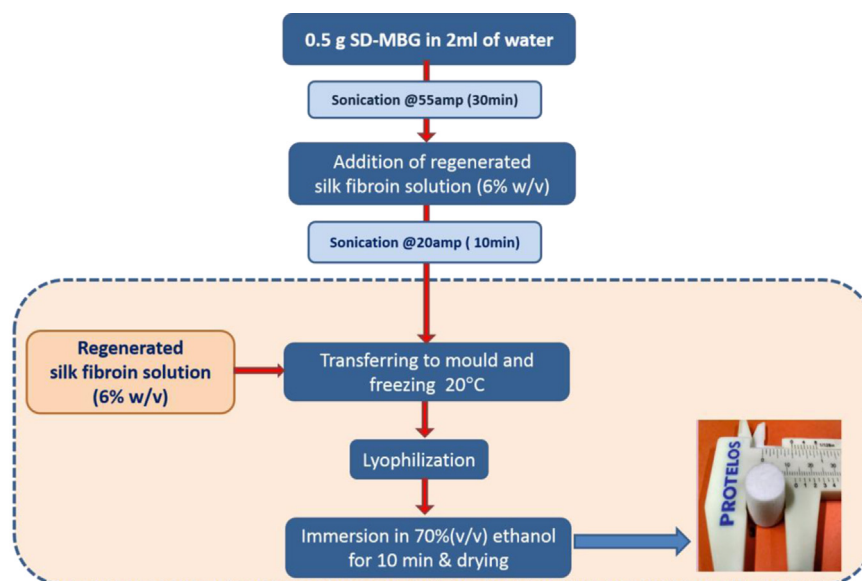


Fig. 1. Preparation of silk/SD-MBG based composite scaffold and silk based scaffold (dotted box).

when using flammable solvents. The collected powder was calcined at 700 °C for 5 h. SD-MBG particle morphology was analyzed with field emission scanning electron microscope (FESEM – SUPRA™ 40, Zeiss) equipped with Energy Dispersive Spectroscopy (EDS).

2.2.3. Preparation of composite scaffolds by freeze-drying

For the preparation of the composite silk/SD-MBG scaffolds, 0.1 g of SD-MBG powders was dispersed in 2 mL of deionized water and sonication was performed at 55% amplitude for 30 min. The RSF solution (6% w/v) was added to the dispersed SD-MBG powders (silk:SD-MBG ratio 10:1 wt/wt) and sonicated for 10 min at 20% amplitude. Silk scaffold, obtained from 6% w/v RSF solution were used as control. The silk/SD-MBG and silk solutions were poured into polystyrene 24 well tissue culture plates (2.5 mL for each scaffold), allowed to dry overnight at 20 °C and then freeze-dried for 3 days to obtain porous scaffolds. The scaffolds were then treated with 70%(v/v) ethanol for 10 min to induce stable β -crystalline structures. The schematic diagram of the followed experimental procedure is shown in Fig. 1.

2.3. Characterisation methods

2.3.1. Characterisation of SD-MBG powders

Nitrogen adsorption measurements at 77 K were performed using a Quantachrome Autosorb 1. Samples of SD-MBG powders were outgassed at 423 K for 5 h before analysis. BET specific surface area has been calculated in the relative pressure range 0.04–0.1 and the pore size has been evaluated through the DFT (Density Functional Theory) method.

Particle size distribution of the sprayed sample was measured using a Particle Sizer Malvern 3600D particle size analyzer. Before the analysis, the powders were dispersed in water and sonicated for 10 min

2.3.2. Characterisation of the porous scaffolds

2.3.2.1. Attenuated Total Reflectance–Fourier Transform Infrared Spectroscopy (ATR-FTIR). Attenuated Total Reflectance–Fourier Transform Infrared Spectroscopy (ATR-FTIR) was performed in the range of 4000–600 cm^{-1} using Perkin Elmer Spectrum 100 UATR KRS5 (Perkin Elmer, Milan) equipped with diamond crystal. The samples were placed over the crystal and pressed to optimum

level to obtain the spectrum. The spectrum, obtained as a result of 16 scans with a resolution of 4 cm^{-1} , was analyzed with the Perkin Elmer Spectrum software.

2.3.2.2. Porosity measurement. The height and diameter of the samples were precisely measured by digital caliper at various points of the sample and the average values were used for the calculation of the scaffold volume. The porosity of the scaffolds was evaluated by geometrical weight–volume method calculated with the following formula.

$$\% \text{ Porosity} = [(V_p/V_s) * 100] \%$$

$$V_p = (V_s - V_m)$$

$$V_m = (W_s/\rho_{\text{silk}})$$

where V_p is the volume of the pores, V_s is the volume of the sample (pores and material), V_m is the volume of the material in the sample, W_s is the weight of the sample, ρ_{silk} is the density of the silk.

Density of the silk is reported as 1.355 g cm^{-3} [34]. The presence of the inorganic phase was not considered in the calculation as the density of the mesoporous bioactive glass is not precisely known and difficult to evaluate but it is not much dissimilar to the silk one. The analysis was repeated for at least four samples.

2.3.2.3. Field emission scanning electron microscope (FESEM). Field emission scanning electron microscope (FESEM – SUPRA™ 40, Zeiss) equipped with Energy Dispersive Spectroscopy (EDS) was utilized to analyze the scaffold morphology. The scaffolds were sliced with razor blade into small cube piece with the volume in the range of 2 mm^3 , fixed on the aluminum stub using carbon tape and sputter coated with silver.

For pore size evaluation, 20 random pores from at least 3 FES-EM images were analyzed by ImageJ software.

2.3.2.4. Micro-computed tomography (micro-CT). The scaffolds were investigated by micro computed tomography (micro-CT, Skyscan 1174) to investigate their structure and the dispersion of the mesoporous powder in the composite samples. For the analysis the following parameters were used: 50 kV, 800 μA , 1200 ms

of exposure time and 6.5 μm of resolution. The 3D structure of the scaffolds was reconstructed using NRecon software.

2.3.2.5. Contact angle measurement. The composite and silk scaffolds were sliced in disc shaped pieces with razor blade to obtain an even surface. 5 mL disposable syringe is used to trickle a drop of water on the evenly cut surface of the scaffold. The droplet was imaged with a camera and the image was processed with dropsnake analysis plugin of ImageJ 1.48 V software to obtain the contact angle. A minimum of five analyses was performed on each sample.

2.3.2.6. Mechanical analysis. The mechanical properties of the composite and silk scaffolds were measured through compression test performed using a mechanical testing machine (MTS, QTest/10). Test specimens were cylinder-shaped scaffolds with 14 mm diameter and an average height of around 10–12 mm measured by means of a digital caliper. Five samples were evaluated for each type of scaffold. The samples were tested at room temperature. A 500N load cell was utilized to perform the analysis. The crosshead speed was set at 0.6 mm min⁻¹ and the load was applied until the specimen was compressed to approximately 80% of its original length. The compressive stress–strain curves were thus obtained and the average elastic modulus (E^*), collapse modulus (E'), collapse strength (σ^*) and strain (ϵ^*), with their standard deviation were calculated for each sample type. The elastic modulus was determined as the slope of the initial linear elastic region of the stress–strain curve, while the collapse modulus as the slope of the collapse plateau region. The collapse strength and strain were determined as the maximum force at the yield point (i.e. end of the elastic region). At least five analyses were performed on each sample type.

2.3.2.7. In vitro bioactivity test. The silk/SD-MBG and silk cylindrical scaffolds were sliced with razor blade into 2 mm thick disks (about 14 mm diameter). The disks were cut in half and the obtained samples were soaked into simulated body fluid (SBF) up to 28 days at 37 °C. SBF was prepared by the protocol reported elsewhere [35]. The refresh of SBF solution was performed twice a week in order to simulate the natural turnover of the physiological fluids. The samples were removed from SBF at various time intervals (3 h, 1 day, 7 days, 14 days and 28 days), gently washed with deionized water and allowed to dry at room temperature. The samples were then analyzed with FESEM and ATR-FTIR to study the formation of hydroxyapatite.

2.3.2.8. In vitro cell test. In vitro cell tests were performed on both silk and silk/SD-MBG scaffolds. Before cell seeding, samples ($\phi \sim 1.2$ cm diameter disks) were sterilised under UV light for 4 h (each side) in 24-well plates, washed several times in PBS, and incubated with 0.5 mL foetal calf serum (FCS) for 30 min. The FCS was then discarded. Bone marrow stromal cells (BMSCs) from rats were grown in a controlled atmosphere (5% CO₂; T = 37 °C) in Iscove's modified Dulbecco's medium (DMEM) supplemented with 10% foetal calf serum (Sigma-Aldrich), 2 mM L-glutamine (Sigma-Aldrich), penicillin (100 U/mL), and streptomycin (100 $\mu\text{g}/\text{mL}$; Sigma-Aldrich) and 0.1 mM nonessential amino acids (NEAA, Lonza, UK) for 1 week. Cells from up to two passages were used for all experiments. A total of 50,000 cells for each scaffolds were seeded onto the film specimens in 1 mL DMEM and were allowed to adhere and proliferate up to 6 days.

After culturing cells for 1, 3 and 6 days, the medium was removed and the samples were transferred to new multiwell plates; 10% PrestoBlue solution (5 mg/mL in DMEM; Fisher Scientific) was added to the cell monolayers; the multiwell plates were incubated at 37 °C for an additional 1 h. After discarding the supernatants,

the dark blue solution was removed (0.2 mL) and quantified spectrophotometrically at 560 nm (Leica DM2500). The results are reported as fluorescent unit. The mean and the standard deviations were obtained from five different experiments.

The BMSCs differentiation was studied after 14 days of cell seeding in osteogenic cell culture medium (added after 7 days of cell culture with the same composition of the standard medium plus 50 $\mu\text{g}/\text{mL}$ ascorbic acid (Sigma-Aldrich), 10 mM β -glycerophosphate (Fluka Biochemika) and 10–8 M dexamethasone (Sigma-Aldrich)). ALP activity was measured by incubating 100 μL of each samples with 0.5 mL alkaline buffer solution (Sigma-Aldrich) and 0.5 mL of stock substrate solution (40 mg p-nitrophenyl phosphate disodium, Sigma-Aldrich), diluted in 10 mL of distilled water, at 37 °C for 1 h. Production of p-nitrophenol in the presence of ALP was measured by monitoring light absorbance of the solution at 410 nm using a Perkin Elmer Lambda 25 UV/Vis Spectrometer. The mean and the standard deviation were obtained from three different experiments. Alkaline phosphatase absorbance values were normalized for cell number calculated using the PicoGreen[®] dsDNA reagent (Invitrogen, USA).

3. Results

3.1. Spray dried mesoporous bioactive glass

FESEM image of the sprayed MBG (Fig. 2) shows well defined, smooth and slightly aggregated micrometric spheres, mostly ranging between 2 μm and 5 μm . No collapsed or broken spheres can be observed. The EDS analysis carried out on the sample confirms a Si/Ca ratio, as average of three measurements, of 3.7, very close to the nominal ratio used in the synthesis.

A type IV N₂ sorption isotherm is observed for SD-MBG, with a hysteresis loop corresponding to the filling of mesopores (Fig. 3). Related specific surface area, obtained by BET model, average pore size and pore volume resulted to be respectively ca 215 m² g⁻¹, ca 5 nm and 0.21 cm³ g⁻¹.

Particle size analysis on SD-MBG (Fig. 4) confirmed the narrow size distribution of the powders, centered at mean diameter of 2.7 μm , with a minor contribution due to aggregates at around 10–12 μm .

3.2. Physico chemical characterisation of porous scaffolds

The process of freeze-drying was utilized in this study for the preparation of silk and composite silk/SD-MBG scaffolds as shown in Fig. 1. FESEM analysis was used to study the scaffold morphology as a function of silk and SD-MBG concentration. The cross-sectional FESEM images of 6% silk scaffolds and silk/SD-MBG composite scaffolds prepared by freeze-drying technique are shown in Fig. 5. The interconnected porous 3D architecture was observed in both silk and silk/SD-MBG composite scaffolds with the pore size of 145 \pm 20 μm and 153 \pm 23 μm , respectively.

The porosity of the scaffolds was evaluated by geometrical weight–volume method by finding the volume of the scaffolds with the height and diameter of the scaffolds. The mean porosity value of silk and silk/SD-MBG composite scaffolds was 88.8 \pm 0.5 vol% and 89.5 \pm 0.1 vol% respectively, showing very high porosity of the scaffolds. There is no significant variation in porosity between the two scaffolds. Silk scaffolds showed smooth trabeculae (Fig. 5(b)) whereas the composite scaffold showed the SD-MBG particles embedded in the trabeculae (Fig. 5(d)) and hence an increase in surface roughness. The SD-MBG addition did not cause significant variation of pore size and porosity of the scaffolds.

Furthermore, the scaffolds were also analyzed with micro-CT to study their 3D architecture. In Fig. 6 it is possible to see both the

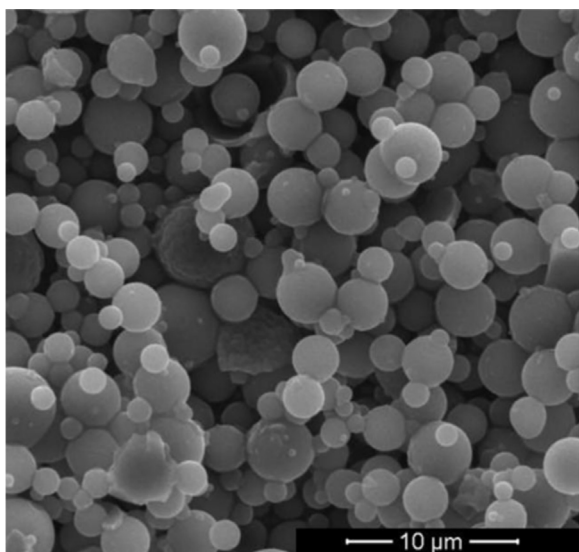


Fig. 2. FESEM image of calcined SD-MBG.

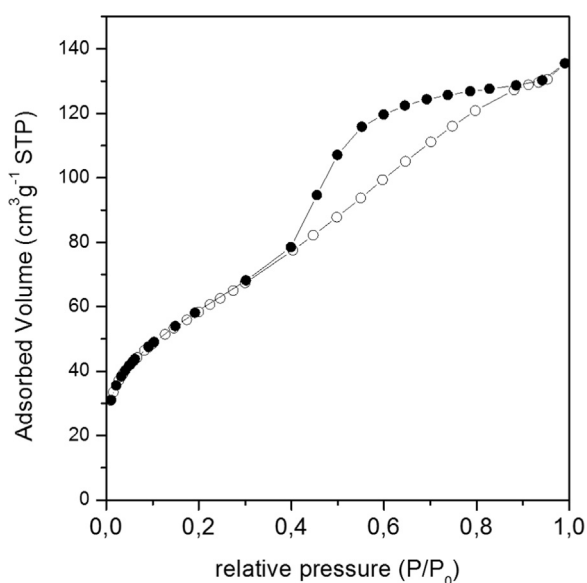


Fig. 3. N₂ adsorption-desorption isotherm at 77 K on SD-MBG.

reconstructed 3D volume and the projections in the three planes of the silk (Fig. 6(a)) and silk/SD-MBG composite (Fig. 6(b)) scaffolds. Micro-CT results demonstrated that the scaffolds showed highly interconnected porosity; however it was possible to verify, under the limitation of micro-CT resolution ($6.5 \mu\text{m}$), that there were no agglomerates of mesoporous spheres, indicating homogeneous distribution of SD-MBG particles in the composite scaffolds.

ATR-FTIR spectra of 6% silk and silk/SD-MBG composite scaffolds before and after ethanol treatment are reported in Fig. 7. Infrared absorption spectrum of the scaffolds shows characteristic absorption peaks assigned to the peptide bonds ($-\text{CONH}-$) that give rise to amide I, amide II and amide III signature peaks. Amide I band ($1700\text{--}1600 \text{ cm}^{-1}$) of the vibrational spectra represents CO stretching mode; amide II band ($1540\text{--}1520 \text{ cm}^{-1}$) is attributed to the bending of NH band associated with CN stretching and amide III ($1300\text{--}1220 \text{ cm}^{-1}$) is due to the in phase combination of CN and CO stretching [36]. The amide I, amide II and amide III bands for untreated silk and silk/SD-MBG based scaffolds were seen at 1642 cm^{-1} , 1520 cm^{-1} and 1230 cm^{-1} respectively. After ethanol

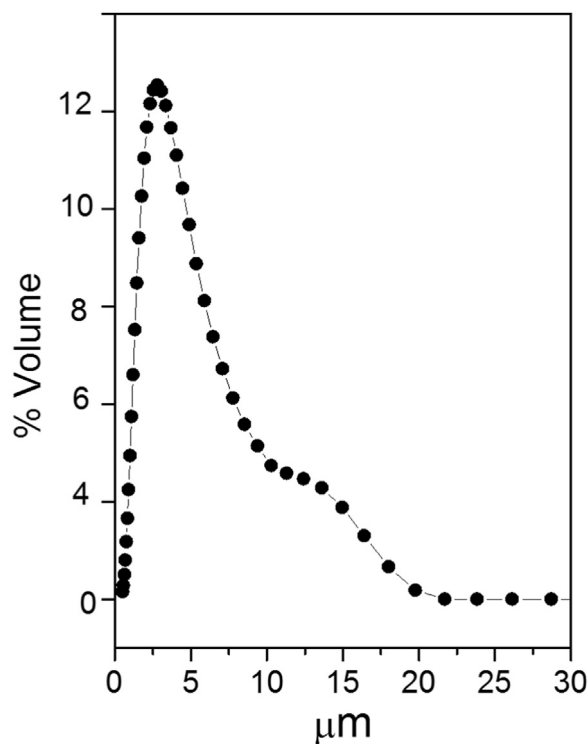


Fig. 4. Particle size distributions of SD-MBG.

treatment, FTIR spectra of amide I, amide II and amide III band shifted to 1620 cm^{-1} , 1510 cm^{-1} , 1220 cm^{-1} respectively. A signal at 1700 cm^{-1} is exclusively observed for ethanol treated samples.

Fig. 8 shows an example of the stress-strain curve obtained for silk and silk/SD-MBG (10/1) composite scaffolds by the excessive compression test at strain of 0–80%. The scaffolds underwent densification upon compression and did not show any fracture in the material. The curves were classified in three distinct regions: linear elastic, collapse plateau, and densification regime [37]. The values of elastic modulus (E^*), collapse modulus (E'), collapse strength (σ^*) and strain (ϵ^*) were calculated from the stress-strain curves and are listed in Table 1. The elastic moduli of the silk and silk/SD-MBG scaffolds are $1.1 \pm 0.2 \text{ MPa}$ and $6.9 \pm 1.0 \text{ MPa}$ and the values of the compressive strength are $0.5 \pm 0.05 \text{ MPa}$ and $0.9 \pm 0.2 \text{ MPa}$, respectively, showing a noticeable increase for the composite compared to the silk-based scaffold.

The surface wettability was assessed by measuring the water contact angle on the surface of the scaffolds. The contact angle of the silk and the silk/SD-MBG composite scaffolds were respectively $105.3^\circ \pm 1.6^\circ$ and $71.2^\circ \pm 2.9^\circ$ as shown in Fig. 9. The silk/SD-MBG composite scaffolds showed a significant decrease in contact angle compared to the silk scaffolds, which is attributed to the improved hydrophilicity of the embedded bioglass microspheres.

3.3. In vitro bioactivity test

The formation of HA on silk/SD-MBG scaffolds was evaluated with FESEM analysis (Fig. 10). HA was visible on the SD-MBG particles after 1-day of incubation (Fig. 10(a)) and a progressive increase in the amount of HA precipitation was observed for prolonged immersion times. Scaffolds incubated for 28 days showed maximum deposition of hydroxyapatite over the scaffold (Fig. 10(e)). As expected, there is no hydroxyapatite formation on pure silk scaffolds as it lacks bioactivity (Fig. 10(f)). The pH of the SBF remained in the range of 7.5 during the whole SBF test for both silk and composite scaffolds. The FTIR analysis performed for the composite scaffolds after SBF treatment showed three main bands

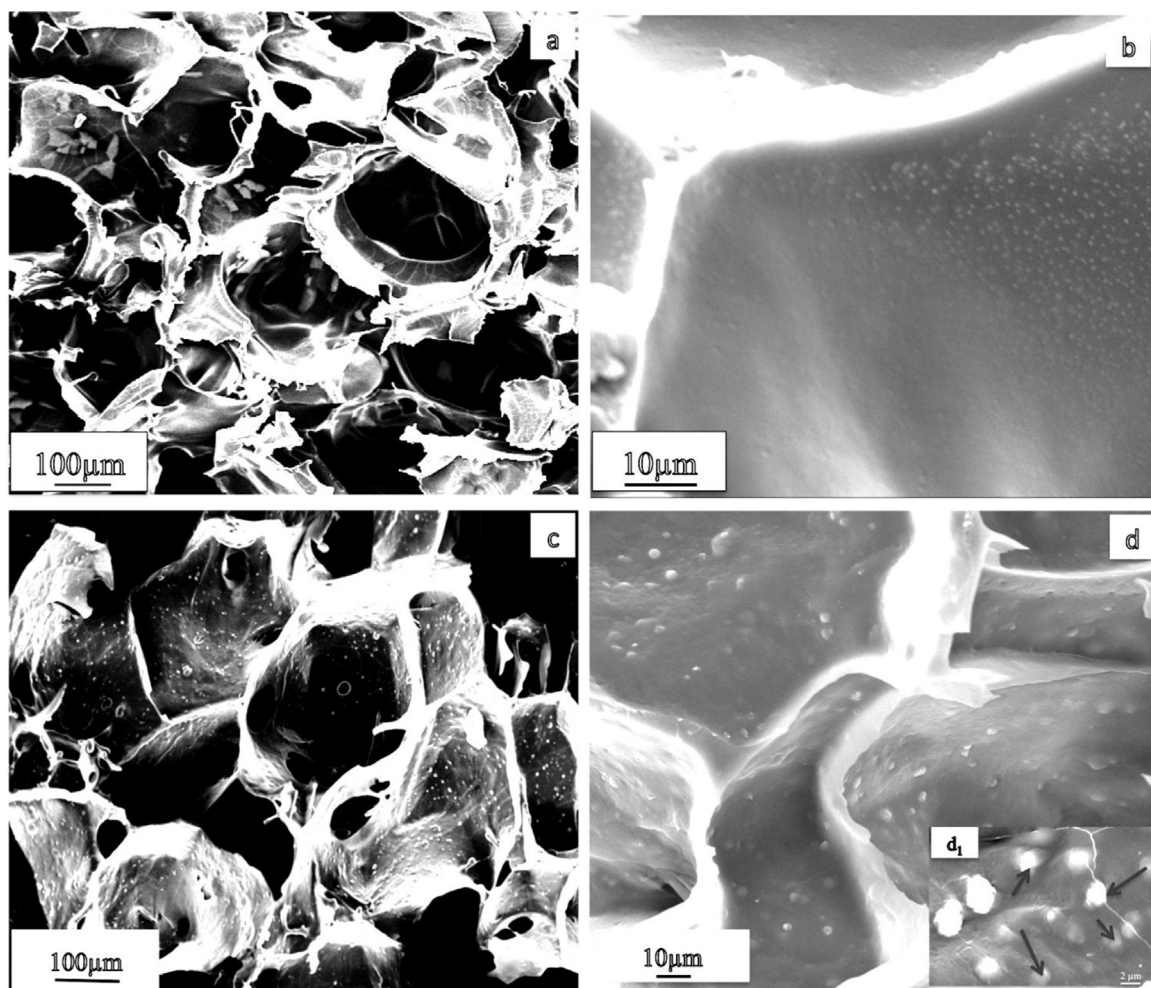


Fig. 5. FESEM image of 6% silk (a, b) and 6% silk/SD-MBG (10:1) wt% composite (c, d) scaffolds prepared by freeze-drying. Arrows indicate the presence of SD-MBG particles embedded in the silk matrix (d_1).

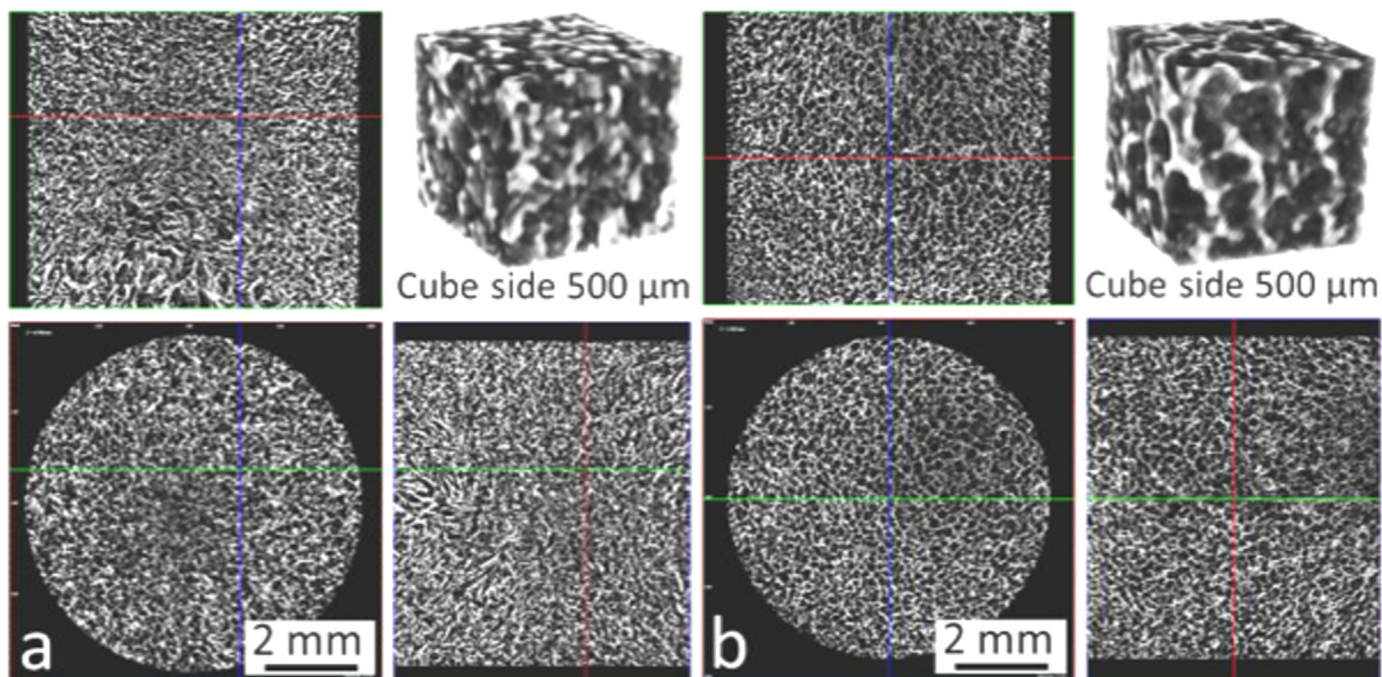


Fig. 6. Micro-CT results showing the projections on the three planes and the 3D model of the structure of (a) 6% silk scaffold and (b) silk/SD-MBG composite scaffold.

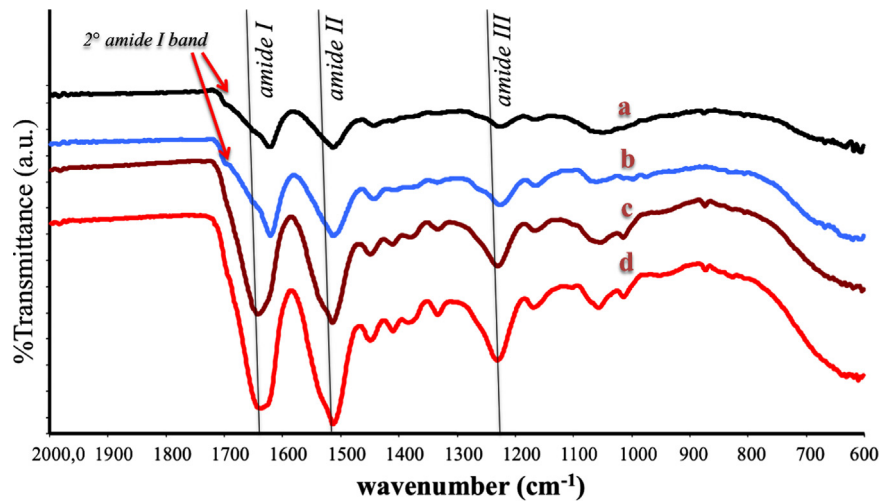


Fig. 7. ATR-FTIR spectra of 6% silk and silk/SD-MBG composite scaffold before and after ethanol treatment showing conformational change. (a) Ethanol treated silk/SD-MBG scaffold, (b) ethanol treated silk scaffold, (c) as prepared silk/SD-MBG scaffold (d) as prepared silk scaffold. Vertical lines in the graph indicate the bands related to amide I, amide II and amide III bands of the untreated scaffolds. The arrows indicate the formation of secondary amide signal after ethanol treatment.

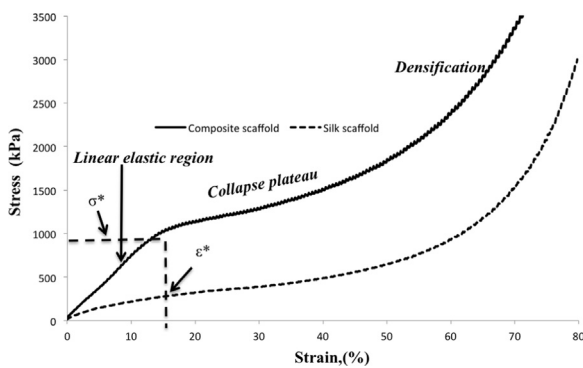


Fig. 8. Examples of stress–strain curves obtained for the porous silk scaffold and composite scaffold compressed at a strain of 0–80%. The crosshead speed was 0.1 mm s⁻¹. The linear elastic region, collapse plateau, and densification region are indicated on the composite scaffold curve. The elastic (E^*) and collapse (E') modulus of the scaffolds have been measured as the slope of the elastic region and collapse plateau, respectively, while the collapse strength (σ^*) and strain (ϵ^*) were calculated as the strength and strain values at the end of the linear elastic region.

Table 1

Elastic modulus (E^*), collapse modulus (E'), collapse strength (σ^*) and strain (ϵ^*) calculated from the corresponding stress–strain curves of silk and silk/SD-MBG scaffolds.

	E^* (MPa)	E' (MPa)	σ^* (MPa)	ϵ^* (%)
Silk scaffolds	1.1 ± 0.2	0.77 ± 0.1	0.21 ± 0.05	13.1 ± 2.8
Silk/SD-MBG composite scaffolds	6.9 ± 1.0	1.74 ± 0.23	0.93 ± 0.18	12.5 ± 0.7

(1035 cm⁻¹, 600 cm⁻¹, 561 cm⁻¹) attributed to phosphate group of the precipitated hydroxyapatite and a significant increase in intensity was found between day 1 (Fig. 11(d)) and day 28 (Fig. 11(e)). Likewise, peaks were observed at 1530–1400 cm⁻¹ and 880 cm⁻¹ that were attributed to the C–O stretching vibrations and C–O out of plane vibrations respectively [37]. Fig. 11(c) shows the FTIR spectra of silk scaffolds after 28 days of SBF immersion where no characteristic phosphate peaks are shown. Fig. 11(a) and (b) are the spectra related to the SD-MBG powders and silk/SD-MBG scaffolds without any SBF treatment, respectively.

EDX analysis on silk/SD-MBG composite was carried out to investigate the presence of calcium and phosphorous and their atomic ratio. The point spectrum obtained for the silk/SD-MBG

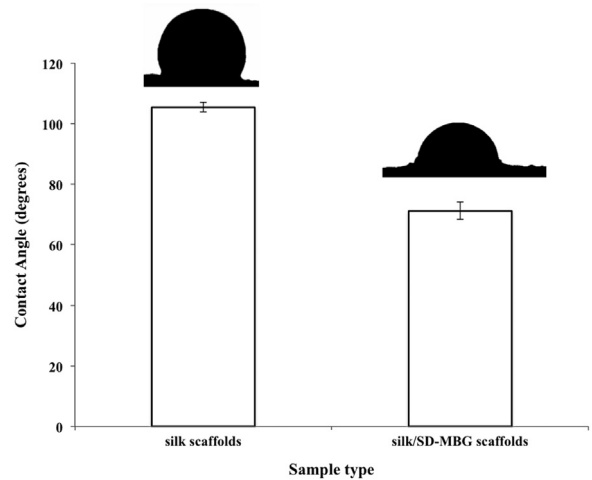


Fig. 9. Contact angle measurements for silk-based scaffold and silk/SD-MBG composite scaffolds.

scaffold (Fig. 12(a) and (b)) after one day of immersion evidenced, for the cauliflower shaped particles precipitated on the scaffold, an atomic ratio Ca/P of 1.63 in close proximity to the biological apatite ratio of 1.67.

Fig. 13(b) shows the EDX spectrum obtained for the investigated area (Fig. 13(a)) of the silk/SD-MBG scaffold after 14 days of soaking in SBF where calcium and phosphate peaks can be seen confirming the presence of hydroxyapatite (sodium and chloride peaks are likely due to residual ions from SBF).

3.4. In vitro cell test

Presto Blue assay was used to evaluate the cells viability on tissue culture plates, which was used as control, and on scaffolds with and without incorporation of SD-MBG powders. The test showed an increase of cell viability along the cell incubation period (Fig. 14). Cell adhesion shows no significant differences between the porous scaffolds at 24 h incubation. The presence of mesoporous glass on the composite scaffold surface enhanced significantly the cell viability compared to their pure counterpart, based on silk, as observed after 3 and 6 days of incubation (relative fluorescence units for porous scaffolds with and without SD-MBG

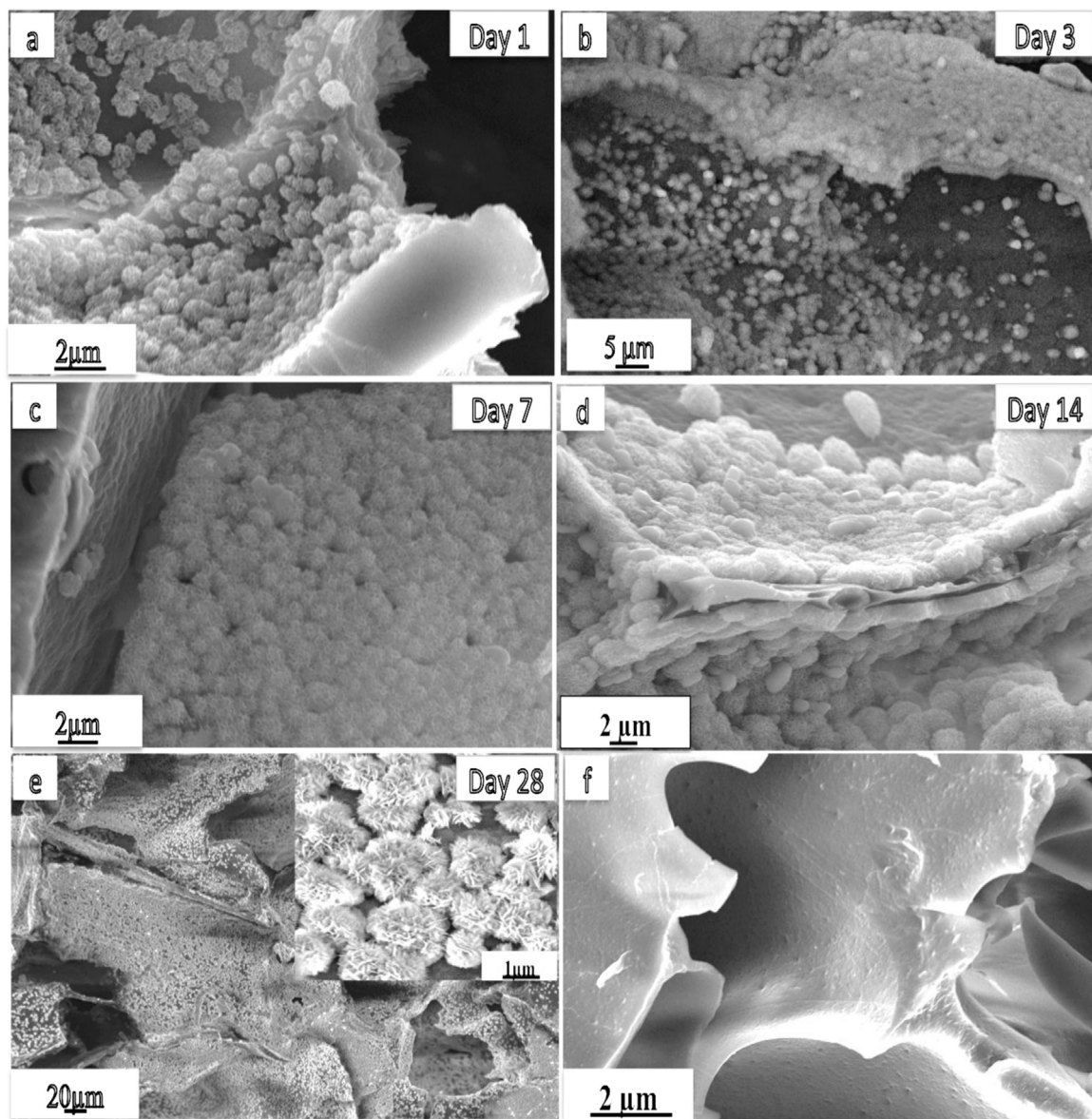


Fig. 10. FESEM images of the silk/SD-MBG based composite scaffold after immersion in SBF after (a) 1 day, (b) 3 days (c) 7 days (d) 14 days (e) 28 days; (f) silk scaffold (control, 28 days).

incorporation were 6657 ± 334 and 6018 ± 129 after 6 days of cells seeding). Moreover, the presence of the SD-MBG particles resulted in slightly lower cell viability compared to the control, polystyrene tissue culture plates, after 4 days (RFUs for the control and the composite scaffold were 6428 ± 241 and 5794 ± 252 respectively) of cell seeding, showing good biocompatibility of the silk/SD-MBG scaffolds. This also confirms that the processes of migration, adhesion and proliferation within the porous scaffolds were not interfered.

Alkaline phosphatase activity was measured to assess the differentiating osteogenic activity of the cell constructs. This test is based on the production of p-nitrophenol in the presence of ALP, measured by monitoring light absorbance of the solution at 410 nm, using a spectrophotometer. As shown in Fig. 15, the higher ALP activity detected in silk/SD-MBG samples in comparison with pure silk scaffolds is ascribed to a positive effect of the MBG particles, causing a statistically significant increase from 0.108 ± 0.037 to 0.248 ± 0.056 after 14 days of cell culture.

4. Discussion

Fabrication of 3D bone substitutes by combining a natural polymer and a bioceramic, as found in bone, can provide massive benefits both in mechanical and biological perspective. In this study, we utilized SD-MBG particles as a means of reinforcement for improving the mechanical and biological properties of biodegradable 3D silk fibroin based scaffolds. Mesoporous bioactive glass particles with spherical shape and narrow size distribution with the mean size of $2.7 \mu\text{m}$ were successfully synthesized by combining the sol-gel method with the aerosol-assisted spray drying technique. The spherical morphology allowed the SD-MBG particles to be uniformly dispersed in the silk fibroin matrix without the formation of large aggregates, as evidenced from the micro-CT, at variance with the use of irregular shaped particles [30].

For bone tissue engineering, the porosity, the pore size and the pore distribution are key factors that enhance the process of *in vivo* osteogenesis [39]. The scaffold porosity is mostly influenced

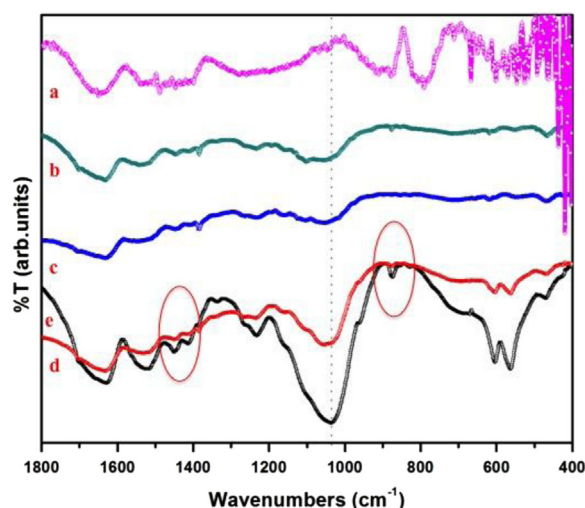


Fig. 11. ATR-FTIR spectra of (a) SD-MBG powders, (b) silk/SD-MBG scaffolds before soaking in SBF, (c) silk scaffolds after soaking in SBF (28 days), (d) silk/SD-MBG scaffolds after a day of SBF soaking, (e) silk/SD-MBG scaffolds immersed in SBF after 28 days.

by the preparation method. Typically scaffolds prepared by freeze-drying technique show porosity values of about 99 vol% [40]. The interconnected pore architecture and high porosity are features of critical importance to ensure cellular penetration within the construct and sufficient supply of nutrients. Moreover the interconnected pores aids in the flushing out of waste products from the scaffold [41]. Finally the porous structure can help the integration of the scaffolds by interlocking with surrounding tissues thus improving its mechanical stability [39]. Mean pore size is an essential aspect for tissue engineering scaffolds as small pore sizes could limit cell migration and vascularization, nutrient diffusion and waste product removal. On the contrary, large pores would reduce the exposed surface area for the attachment of cells [42]. A pore size around 150 μm is suitable for the cell adhesion and migration within the scaffolds [43]. Cell proliferation can be very high if a smaller pore size (100–150 μm) is balanced by an higher porosity (e.g. in the range of 90%) [44]. In accordance with these considerations, the mean pore sizes of the freeze-dried 3D silk and silk/SD-MBG composite scaffolds, measured on the basis of FESEM images, resulted respectively $145 \pm 20 \mu\text{m}$ and $153 \pm 23 \mu\text{m}$, with the mean porosity value of respectively $88.8 \pm 0.5 \text{ vol}\%$ and $89.5 \pm 0.1 \text{ vol}\%$, making them suitable structures for tissue engineering applications. The silk scaffolds exhibited smooth

trabeculae (Fig. 5(b)) at variance with the composite scaffold that, due to the SD-MBG particles embedded in the trabeculae, (Fig. 5(d)) showed a rough surface topography.

FTIR analysis was performed to study the conformational change in the silk fibroin structure after ethanol treatment, which tends to improve the stability of silk fibroin based scaffolds. ATR-FTIR spectra reported in Fig. 7 showed a clear shift of amide I band from 1650 cm^{-1} to 1620 cm^{-1} after ethanol treatment, which confirms the shift of secondary structure from random coil to β -sheet conformation [45]. The secondary band of amide I at about 1700 cm^{-1} , discernible only after ethanol treatment, indicates the formation of anti parallel arrangement of fibroin chains in β -sheet domains in the ethanol treated samples [46,47].

To the best of our knowledge, spherical shaped mesoporous bioactive glass particles have been incorporated with the silk fibroin matrix for the first time and proved to be effective in improving the mechanical properties of the composite scaffolds. Basically, the mechanical behavior of the composite scaffold strongly depends on the size and aspect ratio of the incorporated inorganic phase, the particle-matrix adhesion and the particle amount. The modulus of a composite scaffold can be increased through the incorporation of micro/nano particles while the strength is dependent on the stress transfer between the particle and the matrix [48]. The absence of SD-MBG agglomerates (Fig. 6(b)) is an index of the homogeneous distribution of the glass particles in the silk matrix. Both the uniform distribution of SD-MBG particles and their good cohesion with the silk matrix are most likely responsible for the 4 times increase in collapse strength from 0.2 MPa to 0.9 MPa and for the 7 times increase in the stiffness (i.e. elastic modulus) of the composite compared to the silk-based scaffold (from 1.1 MPa to 6.9 MPa). In the study reported by Wu et al., mesoporous bioactive glasses incorporated into silk scaffolds improved the mechanical properties compared to silk-based homologue. This enhancement was attributed to the presence of nanopores that improved the cohesion between silk and MBG particles [20]. Likewise, the presence of nanochannels in the SD-MBG contributes to the good cohesion of the inorganic phase with the silk solution. The elastic modulus and collapse strength of the silk/SD-MBG are higher compared with the earlier reported values of silk/EISA-MBG composite scaffolds prepared by freeze-drying technique, i.e. ($\sigma^* = 0.42 \text{ MPa}$ and $E^* = 0.7 \text{ MPa}$) [20]. The increase in the mechanical properties can be attributed to the uniform shape and small size of the inorganic phase and the better distribution of the SD-MBG particles within the silk matrix. The inclusion of an inorganic phase showed a slight decrease in the deformability of the silk/SD-MBG composite scaffolds (i.e. collapse

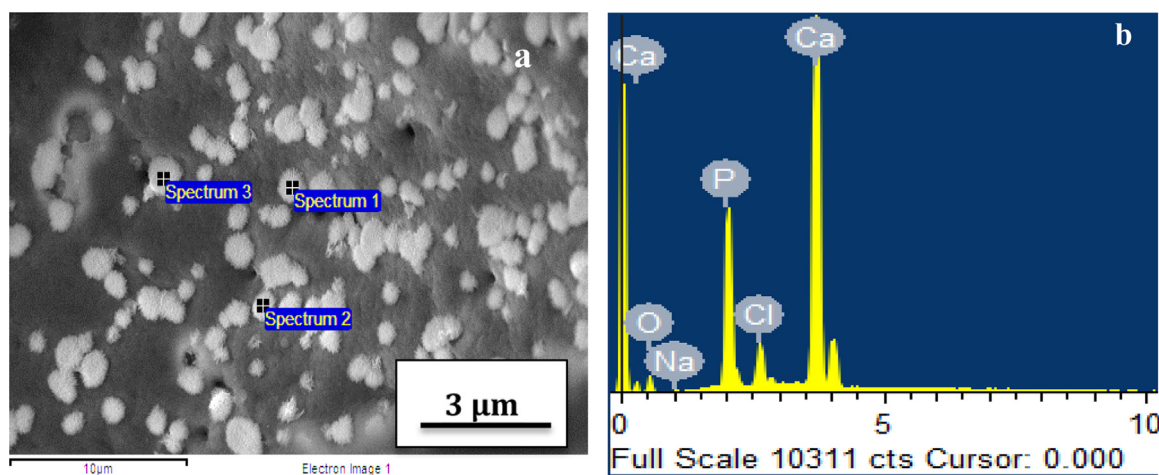


Fig. 12. (a) SEM image of the silk/SD-MBG based composite scaffold after one day immersion in SBF, (b) related punctual EDX analysis.

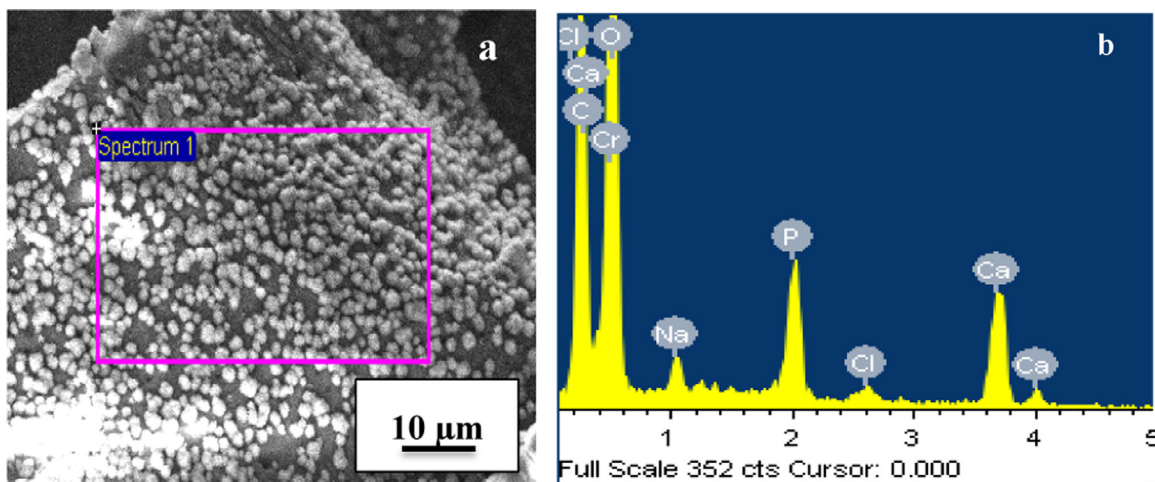


Fig. 13. (a) SEM image of the silk/SD-MBG composite scaffold after 14 days immersion in SBF, (b) related area EDX analysis.

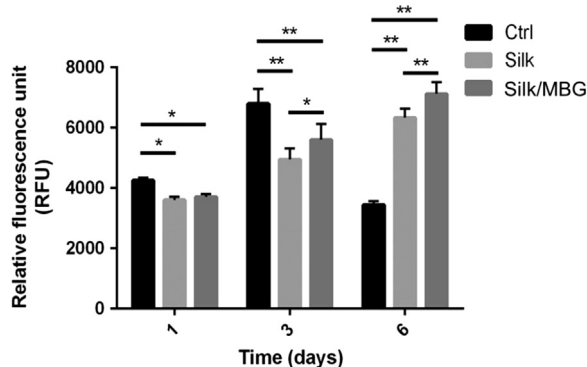


Fig. 14. Biocompatibility studies on silk and silk/SD-MBG based composite scaffolds with rat bone marrow stromal cells (BMSC). Tissue culture plates were used as control.

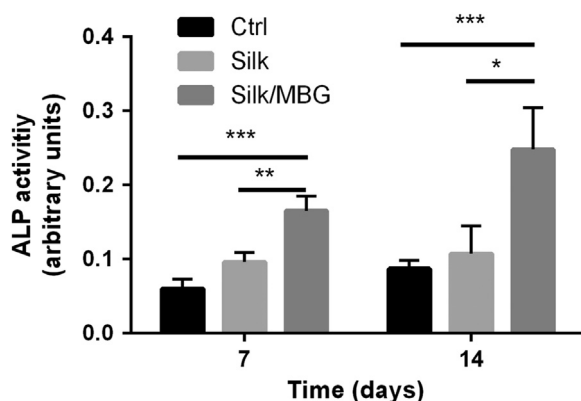


Fig. 15. ALP activity on silk and silk/SD-MBG based composite scaffolds with BMSCs. Tissue culture plates were used as control. The values were normalized for cell number calculated using the PicoGreen[®] dsDNA reagent.

strain) and the collapse modulus is increased twice than that of silk scaffolds. The mechanical property of the silk/SD-MBG scaffolds significantly improved with MBG incorporation. However, the silk-based scaffolds prepared by freeze drying shows very high porosity that causes the lower elastic modulus and collapse strength of the scaffolds than those of the cancellous bone. Hence, these composite scaffolds can be used for non-load bearing applications. In further studies, the scaffolds mechanical properties could be further enhanced by increasing the SD-MBG wt% in the scaffold and/or lowering the scaffold porosity.

Generally, when the contact angle of the material is higher than 90° , it is said to be hydrophobic and if less than 90° is hydrophilic. Cell-material interaction has a crucial role in the adhesion, growth and differentiation of cells in the scaffolds. Cells adhere with the scaffolds through cell/scaffold interface, so the surface characteristics like hydrophobicity, texture and topology are fundamental to have suitable cell response [49]. The contact angle of the silk and the silk/SD-MBG composite scaffolds were found to be $105.3^\circ \pm 1.6^\circ$ and $71.2^\circ \pm 2.9^\circ$ respectively as shown in Fig. 9. The decrease in contact angle in the silk/SD-MBG composite scaffold was attributed to the addition of hydrophilic SD-MBG particles to the silk matrix. Moreover, the addition of SD-MBG increased the trabeculae roughness (Fig. 6(d)), which has influence on the textural property of the scaffolds that might contribute to the decrease in contact angle of the silk/SD-MBG scaffolds [50]. The increase in hydrophilicity of the scaffolds can enhance the adsorption of protein over the surface of the biomaterial and thus being responsible for the increase in cell adhesion [51]. Decrease in the hydrophobicity of the surface can improve the adhesion of osteoblast cells over the surface, which was reported earlier. This shows the incorporation of SD-MBG also helps in reducing the hydrophobic nature of the scaffold thus attracting the cell adhesion [52].

The formation of hydroxyapatite (HA) on the surface of the biomaterial in SBF, whose ion concentrations is nearly equal to those of human blood, is called *in vitro* bioactivity. This study is an important indicator for the *in vivo* bioactivity and the cell-tissue interactions. The silk/SD-MBG scaffolds exhibited an excellent hydroxyapatite forming ability readily in 1 day after immersing in SBF (Fig. 10(a)) and the study was progressed till 28 days resulting in abundant spherical shaped HA formation visible in the scaffolds as evident from the FESEM images (Fig. 10 (b)–(e)). The carbonate band in FTIR spectra started to appear with in a day of immersion in SBF and the sharpness of the band is higher in case of samples immersed for longer period (28 days) that portrays the formation of carbonated hydroxyapatite. The apatite forming ability is attributed to the presence of SD-MBG particles in the composite scaffolds. Scaffolds incubated for 28 days showed maximum deposition of hydroxyapatite over the scaffold (Fig. 10(e)). CaO (20 mol%) in the SD-MBG induces the ionic exchange between Ca^{2+} and H^+ of SBF that increases the silanol on MBG surface, which, subsequently results in biomineralisation. The increase in the hydroxyapatite deposition in the silk/SD-MBG composite scaffolds was due to an increased exposition of SD-MBG particles to the aqueous environment with time. In fact, at the beginning they were totally embedded on the silk matrix, while with time an

increased exposition of SD-MBG particles occurred due to the surface erosion of the silk matrix in the aqueous milieu. As expected there is no hydroxyapatite formation on pure silk scaffolds as it lacks bioactivity, which was confirmed, further with ATR-FTIR results, as there is no spectral bands for phosphate. The EDX spectra (Fig. 12(a)) again confirm the presence of calcium and phosphate in the silk/SD-MBG scaffolds immersed in SBF. In the preliminary studies (Fig. S1), we found the presence of Si peak in the EDX spectrum after a day of immersion of silk/SD-MBG scaffolds and as the day progresses the peak for Si was diminished in 14th day sample as shown in Fig. 13 that results in the thick layer of hydroxyapatite with the dissolution of SD-MBG particles. The molar ratio of Ca/P as per EDX is 1.63 and the values are in reach with the stoichiometric biological apatite [38]. These results confirm that the presence of SD-MBG particles improves the bioactivity of silk-based scaffolds.

Presto Blue assay showed an increase of cell viability along the cell incubation period (Fig. 14). The presence of the SD-MBG particles resulted in slightly lower cell viability compared to the control, polystyrene tissue culture plates, after 4 days of cell seeding, showing good biocompatibility of the silk/SD-MBG scaffolds. This also confirms that the processes of migration, adhesion and proliferation within the porous scaffolds were not interfered. As shown in Fig. 15, the higher ALP activity detected in silk/SD-MBG samples in comparison with pure silk scaffolds is related to a positive effect of the addition of the MBG particles, causing a statistically significant increase from 0.108 ± 0.037 to 0.248 ± 0.056 after 14 days of cell culture.

5. Conclusion

Silk and silk/SD-MBG-based composite scaffolds were prepared by freeze-drying technique. The incorporation of SD-MBG particles improved the physico-chemical and biological properties of the composite scaffolds compared to its pure silk counterpart. The scaffolds have shown highly interconnected pores with very high porosity values and a macroporous architecture that made it a valid candidate for bone tissue engineering scaffold. The mechanical properties of the composite scaffolds showed a significant increase compared to pure silk scaffolds, due to the uniform distribution of the SD-MBG particles. The introduction of SD-MBG particles reduced the contact angle of composite scaffolds and may positively influence the cell-biomaterial interaction. The SD-MBG addition countered the lack of bioactivity of the silk scaffolds inducing the precipitation of hydroxyapatite layer on their surface only after a day of incubation in simulated body fluid. The *in vitro* cell studies showed a good biocompatibility of the scaffolds indicating their potential for use as 3D scaffolds for bone tissue engineering.

Acknowledgements

The author Arunseshan Chandrasekaran sincerely thanks European commission - Heritage program and Council of Scientific and Industrial Research, India for their financial assistance. The authors would like to thank Dr. Lucia Pontiroli for her contribution in the synthesis of the mesoporous bioactive glass powder.

Appendix A. Supplementary material

Supplementary data associated with this article can be found in the online version at <http://dx.doi.org/10.1016/j.ceramint.2016.05.176>.

References

- [1] F. Baino, C. Vitale-Brovarone, Three-dimensional glass-derived scaffolds for bone tissue engineering: current trends and forecasts for the future, *J. Biomed. Mater. Res.: Part A* 97A (2011) 514–535, <http://dx.doi.org/10.1002/jbm.a.33072>.
- [2] J. Rnjak-Kovacina, L.S. Wray, Burke K. a, T. Torregrosa, J.M. Golinski, W. Huang, et al., Lyophilized silk sponges: a versatile biomaterial platform for soft tissue engineering, *ACS Biomater. Sci. Eng.* (2015), <http://dx.doi.org/10.1021/ab500149p>.
- [3] K. Rezwan, Q.Z. Chen, J.J. Blaker, A.R. Boccaccini, Biodegradable and bioactive porous polymer/inorganic composite scaffolds for bone tissue engineering, *Biomaterials* 27 (2006) 3413–3431, <http://dx.doi.org/10.1016/j.biomaterials.2006.01.039>.
- [4] M. Mondal, The silk proteins, sericin and fibroin in silkworm, *Bombyx mori* Linn., a review, *Casp. J. Environ. Sci.* 5 (2) (2007) 63–76.
- [5] M.N. Padamwar, A.P. Pawar, Silk sericin and its applications: a review, *J. Sci. Ind. Res.* 63 (2004) 323–329.
- [6] C.Z. Zhou, F. Confalonieri, M. Jacquet, R. Perasso, Z.G. Li, J. Janin, Silk fibroin: structural implications of a remarkable amino acid sequence, *Proteins* 44 (2001) 119–122 (<http://www.ncbi.nlm.nih.gov/pubmed/11391774>).
- [7] R.L. Horan, K. Antle, A.L. Collette, Y. Wang, J. Huang, J.E. Moreau, et al., In vitro degradation of silk fibroin, *Biomaterials* 26 (2005) 3385–3393, <http://dx.doi.org/10.1016/j.biomaterials.2004.09.020>.
- [8] B.D. Lawrence, J.K. Marchant, M. Pindrus, F. Omenetto, L. Kaplan, Silk film biomaterials for cornea tissue engineering, *Biomaterials* 30 (2009) 1299–1308, <http://dx.doi.org/10.1016/j.biomaterials.2008.11.018>.
- [9] J.G. Hardy, S.A. Geissler, D. Aguilar, M.K. Villancio-Wolter, D.J. Mouser, R. C. Sukhavas, R.C. Cornelison, L.W. Tien, R.C. Preda, R.S. Hayden, J.K. Chow, L. Nguy, D.L. Kaplan, Instructive conductive 3D silk foam-based bone tissue scaffolds enable electrical stimulation of stem cells for enhanced osteogenic differentiation, *Macromol. Biosci.* (2015), <http://dx.doi.org/10.1002/mabi.201500171>.
- [10] H. Perry, A. Gopinath, D.L. Kaplan, L.D. Negro, F.G. Omenetto, Nano- and micro-patterning of optically transparent, mechanically robust, biocompatible silk fibroin films, *Adv. Mater.* 20 (2008) 3070–3072, <http://dx.doi.org/10.1002/adma.200800011>.
- [11] C.J. Bettinger, K. Cyr, A. Matsumoto, R. Langer, J.T. Borenstein, D.L. Kaplan, Silk fibroin microfluidic devices, *Adv. Mater.* 19 (5) (2007) 2847–2850, <http://dx.doi.org/10.1002/adma.200602487>.
- [12] S. Hofmann, H. Hagenmüller, A.M. Koch, R. Müller, G. Vunjak-Novakovic, D. L. Kaplan, et al., Control of in vitro tissue-engineered bone-like structures using human mesenchymal stem cells and porous silk scaffolds, *Biomaterials* 28 (2007) 1152–1162, <http://dx.doi.org/10.1016/j.biomaterials.2006.10.019>.
- [13] J. Kundu, L. a Poole-Warren, P. Martens, S.C. Kundu, Silk fibroin/poly(vinyl alcohol) photocrosslinked hydrogels for delivery of macromolecular drugs, *Acta Biomater.* 8 (2012) 1720–1729, <http://dx.doi.org/10.1016/j.actbio.2012.01.004>.
- [14] E.S. Gil, S.H. Park, X. Hu, P. Cebe, D.L. Kaplan, Impact of sterilization on the enzymatic degradation and mechanical properties of silk biomaterials, *Macromol. Biosci.* 14 (2014) 257–269, <http://dx.doi.org/10.1002/mabi.201300321>.
- [15] L. Yan, J.M. Oliveira, A.L. Oliveira, R.L. Reis, In vitro evaluation of the biological performance of macro/micro-porous silk fibroin and silk-nano calcium phosphate scaffolds, *J. Biomed. Mater. Res. Part B* (2014) 888–898, <http://dx.doi.org/10.1002/jbm.b.33267>.
- [16] L.-P. Yan, A.J. Salgado, J.M. Oliveira, A.L. Oliveira, R.L. Reis, De novo bone formation on macro/microporous silk and silk/nano-sized calcium phosphate scaffolds, *J. Bioact. Compat. Polym.* 28 (2013) 439–452, <http://dx.doi.org/10.1177/0883911513503538>.
- [17] S. Bhumiratana, W.L. Grayson, A. Castaneda, D.N. Rockwood, E.S. Gil, D. L. Kaplan, et al., Nucleation and growth of mineralized bone matrix on silk-hydroxyapatite composite scaffolds, *Biomaterials* 32 (2011) 2812–2820, <http://dx.doi.org/10.1016/j.biomaterials.2010.12.058>.
- [18] H. Liu, G. Wei, Y. Fei, H. Shi, S. Xiong, Y. Wu, et al., Biomaterials Composite scaffolds of nano-hydroxyapatite and silk fibroin enhance mesenchymal stem cell-based bone regeneration via the interleukin 1 alpha autocrine/paracrine signaling loop, *Biomaterials* 49 (2015) 103–112, <http://dx.doi.org/10.1016/j.biomaterials.2015.01.017>.
- [19] N. Cheng, Y. Wang, Y. Zhang, B. Shi, The osteogenic potential of mesoporous bioglasses / silk and non-mesoporous bioglasses/silk scaffolds in ovariectomized rats: in vitro and in vivo Evaluation, *PLoS ONE* 8 (2013) 1–16, <http://dx.doi.org/10.1371/journal.pone.0081014>.
- [20] C. Wu, Y. Zhang, Y. Zhou, W. Fan, Y. Xiao, A comparative study of mesoporous glass/silk and non-mesoporous glass/silk scaffolds: physiochemistry and in vivo osteogenesis, *Acta Biomater.* 7 (2011) 2229–2236, <http://dx.doi.org/10.1016/j.actbio.2010.12.019>.
- [21] C. Wu, Y. Zhang, Y. Zhu, T. Friis, Y. Xiao, Structure-property relationships of silk-modified mesoporous bioglass scaffolds, *Biomaterials* 31 (2010) 3429–3438, <http://dx.doi.org/10.1016/j.biomaterials.2010.01.061>.
- [22] Y. Zhang, M. Rj, S. Li, B. Shi, A. Sculean, C.X. Novel, et al., Novel mesoporous bioGlass / silk scaffold containing adPDGF-B and adBMP7 for the repair of periodontal defects in beagle dogs, *J. Clin. Periodontol.* (2015) 262–271, <http://dx.doi.org/10.1111/jcpe.12364>.
- [23] X. Yan, C. Yu, X. Zhou, J. Tang, D. Zhao, Highly ordered mesoporous bioactive glasses with superior in vitro bone-forming bioactivities, *Angew. Chem. Int. Ed. Engl.* 43 (44) (2004) 5980–5984, <http://dx.doi.org/10.1002/anie.200460598>.

- [24] M. Vallet-Regí, F. Balas, D. Arcos, Minireviews mesoporous materials for drug delivery, *Angew. Chem. Int. Ed. Engl.* (2007) 7548–7558, <http://dx.doi.org/10.1002/anie.200604488>.
- [25] F. Baino, S. Fiorilli, R. Mortera, B. Onida, E. Saino, L. Visai, et al., Mesoporous bioactive glass as a multifunctional system for bone regeneration and controlled drug release, *J. Appl. Biomater. Biomech.* 10 (1) (2012) 12–21, <http://dx.doi.org/10.5301/JABB.2012.9036>.
- [26] C. Wu, Y. Zhang, Y. Zhou, W. Fan, Y. Xiao, A comparative study of mesoporous glass / silk and non-mesoporous glass/silk scaffolds : physiochemistry and in vivo osteogenesis, *Acta Biomater.* 7 (2011) 2229–2236, <http://dx.doi.org/10.1016/j.actbio.2010.12.019>.
- [27] Z. Xiaoxin, Z. Jiayin, S.H.I. Bin, Mesoporous Bioglass, Mesoporous bioglass/silk fibroin scaffolds as a drug delivery system : fabrication, drug loading and release in vitro and repair calvarial defects in vivo, *J. Wuhan. Univ. Technol.: Mater. Sci. Ed.* 29 (2014) 401–406, <http://dx.doi.org/10.1007/s11595-014-0929-0>.
- [28] W.Y. Choi, H.E. Kim, M.J. Kim, U.C. Kim, J.H. Kim, Y.H. Koh, Production and characterization of calcium phosphate (CaP) whisker-reinforced poly(ϵ -caprolactone) composites as bone regenerative, *Mater. Sci. Eng. C* 30 (2010) 1280–1284, <http://dx.doi.org/10.1016/j.msec.2010.07.018>.
- [29] J.H. Jo, E.J. Lee, D.S. Shin, H.E. Kim, H.W. Kim, Y.H. Koh, et al., In vitro/in vivo biocompatibility and mechanical properties of bioactive glass nanofiber and poly(ϵ -caprolactone) composite materials, *J. Biomed. Mater. Res.: Part B Appl. Biomater.* 91 (2009) 213–220, <http://dx.doi.org/10.1002/jbmb.b.31392>.
- [30] B. Lei, K.H. Shin, D.Y. Noh, Y.H. Koh, W.Y. Choi, H.E. Kim, Bioactive glass microspheres as reinforcement for improving the mechanical properties and biological performance of poly(ϵ -caprolactone) polymer for bone tissue regeneration, *J. Biomed. Mater. Res.: Part B Appl. Biomater.* 100B (2012) 967–975, <http://dx.doi.org/10.1002/jbmb.b.32659>.
- [31] D. Arcos, a López-Noriega, E. Ruiz-Hernández, O. Terasaki, M. Vallet-Regí, Ordered mesoporous microspheres for bone grafting and drug delivery, *Chem. Mater.* 21 (2009) 1000–1009, <http://dx.doi.org/10.1021/cm801649z>.
- [32] C. Vitale-Brovarone, L. Pontiroli, G. Novajra, I. Tcacencu, J.C. Reis, A. Manca, Spine-ghost: a new bioactive cement for vertebroplasty, *Key Eng. Mater.* 631 (2014) 43–47, <http://dx.doi.org/10.4028/www.scientific.net/KEM.631.43>.
- [33] H.Y. Wang, Y.Q. Zhang, Effect of regeneration of liquid silk fibroin on its structure and characterization, *Soft Matter* (2012) 138–145, <http://dx.doi.org/10.1039/c2sm26945g>.
- [34] R. Rajkhowa, E.S. Gill, J. Kluge, K. Numara, L. Wang, X. Wang, D.L. Kaplan, Reinforcing silk scaffolds with silk particles, *Macromol. Biosci.* 10 (6) (2010) 599–611, <http://dx.doi.org/10.1002/mabi.200900358>.
- [35] T. Kokubo, H. Takadama, How useful is SBF in predicting in vivo bone bioactivity, *Biomaterials* 27 (2006) 2907–2915, <http://dx.doi.org/10.1016/j.biomaterials.2006.01.017>.
- [36] N. Bhardwaj, W.T. Sow, D. Devi, K.W. Ng, B.B. Mandal, N. Cho, Silk fibroin-keratin based 3D scaffolds as a dermal substitute for skin tissue engineering, *Integr. Biol.* 7 (2014) 53–63, <http://dx.doi.org/10.1039/C4IB00208C>.
- [37] P. Gentile, M. Mattioli-Belmonte, V. Chiono, C. Ferretti, F. Baino, C. Tonda-Turo, et al., Bioactive glass/polymer composite scaffolds mimicking bone tissue, *J. Biomed. Mater. Res.: Part A* 100A (2012) 2654–2667, <http://dx.doi.org/10.1002/jbm.a.34205>.
- [38] G.A. Stanciu, I. Sandulescu, B. Savu, S.G. Stanciu, K.M. Paraskevopoulos, X. Chatzistavrou, et al., Investigation of the hydroxyapatite growth on bioactive glass, *J. Biomed. Pharm. Eng.* 1 (2007) 34–39.
- [39] V. Karageorgiou, D.L. Kaplan, Porosity of 3D biomaterial scaffolds and osteogenesis, *Biomaterials* 26 (2005) 5474–5491, <http://dx.doi.org/10.1016/j.biomaterials.2005.02.002>.
- [40] R. Nazarov, H.-J. Jin, D.L. Kaplan, Porous 3-D scaffolds from regenerated silk fibroin, *Biomacromolecules* 5 (2004) 718–726, <http://dx.doi.org/10.1021/bm034327e>.
- [41] F.J. O'Brien, Biomaterials & scaffolds for tissue engineering, *Mater. Today* 14 (2011) 88–95, [http://dx.doi.org/10.1016/S1369-7021\(11\)70058-X](http://dx.doi.org/10.1016/S1369-7021(11)70058-X).
- [42] C.M. Murphy, F.J. O'Brien, Understanding the effect of mean pore size on cell activity in collagen-glycosaminoglycan scaffolds, *Cell Adhes. Migr.* 6 (2010) 377–381, <http://dx.doi.org/10.4161/cam.4.3.11747>.
- [43] C.M. Murphy, M.G. Haugh, F.J.O. Brien, The effect of mean pore size on cell attachment, proliferation and migration in collagen – glycosaminoglycan scaffolds for bone tissue engineering, *Biomaterials* 31 (2010) 461–466, <http://dx.doi.org/10.1016/j.biomaterials.2009.09.063>.
- [44] Q.L. Loh, C. Choong, D. Oxon, M. Hons, Three-dimensional scaffolds for tissue engineering applications: role of porosity and pore size, *Tissue Eng. Part B: Rev.* 19 (2013) 485–502, <http://dx.doi.org/10.1089/ten.teb.2012.0437>.
- [45] X. Chen, Z. Shao, N.S. Marinkovic, L.M. Miller, P. Zhou, M.R. Chance, Conformation transition kinetics of regenerated *Bombyx mori* silk fibroin membrane monitored by time-resolved FTIR spectroscopy, *Biophys. Chem.* 89 (2001) 25–34, [http://dx.doi.org/10.1016/S0301-4622\(00\)00213-1](http://dx.doi.org/10.1016/S0301-4622(00)00213-1).
- [46] G. Freddi, G. Pessina, M. Tsukada, Swelling and dissolution of silk fibroin (*Bombyx mori*) in N-methylmorpholine N-oxide, *Int. J. Biol. Macromol.* 24 (1999) 251.
- [47] G.M. Nogueira, C.D. Rodas, C.P. Leite, C. Giles, O.Z. Higa, B. Polakiewicz, et al., Preparation and characterization of ethanol-treated silk fibroin dense membranes for biomaterials application using waste silk fibers as raw material, *Bioresour. Technol.* 101 (2010) 8446–8451, <http://dx.doi.org/10.1016/j.biortech.2010.06.064>.
- [48] S. Fu, X. Feng, B. Lauke, Y. Mai, Effects of particle size, particle / matrix interface adhesion and particle loading on mechanical properties of particulate – polymer composites, *Compos. Part B: Eng.* 39 (2008) 933–961, <http://dx.doi.org/10.1016/j.compositesb.2008.01.002>.
- [49] Y. Mei, K. Saha, S.R. Bogatyrev, J. Yang, A.L. Hook, Z.I. Kalciglu, et al., Combinatorial development of biomaterials for clonal growth of human pluripotent stem cells, *Nat. Mater.* 9 (2010) 768–778, <http://dx.doi.org/10.1038/NMAT2812>.
- [50] H. Zhu, B. Wu, X. Feng, J. Chen, Preparation and characterization of bioactive mesoporous calcium silicate – silk fibroin composite films, *J. Biomed. Mater. Res. B Appl. Biomater.* (2011) 330–341, <http://dx.doi.org/10.1002/jbm.b.31856>.
- [51] R. Ayala, C. Zhang, D. Yang, Y. Hwang, A. Aung, S.S. Shroff, et al., Engineering the cell e material interface for controlling stem cell adhesion, migration, and differentiation, *Biomaterials* 32 (2011) 3700–3711, <http://dx.doi.org/10.1016/j.biomaterials.2011.02.004>.
- [52] J. Wei, T. Igarashi, N. Okumori, T. Igarashi, Influence of surface wettability on competitive protein adsorption and initial attachment of osteoblasts, *Biomed. Mater.* 045002 (2009) 1–7, <http://dx.doi.org/10.1088/1748-6041/4/4/045002>.